Front. Optoelectron. 2020, 13(3): 291–302
https://doi.org/10.1007/s12200-020-1045-8

RESEARCH ARTICLE

A corona modulation device structure and mechanism based on perovskite quantum dots random laser pumped using an electron beam

Yan ZHU, Yining MU (✉), Fanqi TANG, Peng DU, Hang REN

School of Science, Changchun University of Science and Technology, Changchun 130022, China

Abstract Although laser pumping using electron beam (EB) has high transient power output and easy modulation based on perovskite quantum dot (PQD) film, its lasing emitting direction is the same as the pumped EB's direction. Thus, realizing the conventional direct device structure through the film lasing mechanism is extremely difficult. Therefore, using the random lasing principle, herein, we proposed a corona modulation device structure based on PQDs random laser pumped using an EB. We discussed and stimulated the optimized designed method of the device in terms of parameters of the electronic optical device and the utilization ratio of output power and its modulation extinction ratio, respectively. According to the simulation results, this type of device structure can effectively satisfy the new random lasing mechanism in terms of high-speed and high-power modulation.

Keywords corona, modulation, perovskite quantum dot (PQD), random laser, electron beam (EB)

1 Introduction

Perovskite quantum dot (PQD) material exhibits highly external quantum efficiency, excellent exciton confinement, and short carrier lifetime that are superior to conventional luminescence materials [1–5], which has effectively attracted research attention in the luminescence field [6–10]. Currently, an increasing number of distinguished studies have reported PQD optical pumping laser and electric injection through light-emission. In addition, with the rapid development in PQD material manufacturing and gradual improvement of the device's theory, some scholars have studied PQD emitting light devices for visual optical communication. For example, white light by electric injection that reaches 10.9% of external quantum efficiency has been realized using trichromatic hybrid halide PQDs [11]. PQD light-emitting diodes (LEDs) with an external quantum efficiency has exceeded 20% and its lifespan has been nearly 100 h too [12]. Changing the ligands of PQDs, the laser threshold was reduced and the stability of the material was improved [13]. However, as a typical semiconductor device structure, an inherent technology paradox exists between the LED's output power and modulation bandwidth. Namely, the cross-sectional area of the LED junction is directly and inversely proportional to the output power and modulation bandwidth, respectively, which generates the power gain-bandwidth product constraint [14–16]. Hence, the constraint will substantially limit the PQD LED's transient characteristics in the communication field.

Furthermore, PQD optical-pumping is a cutting-edge nad popular research subject. For example, Saudi scientists utilized PQDs as color converters to generate warm white light via blue laser irradiation and became the first to realize high-speed digital communication testing whose modulation bandwidth is around several hundred MHz [17]. Soon after, *Nature* reported in 2018 that a lead-free alloyed perovskite can stably emit white light via optical pumping [18]. However, the modulation characteristics of PQD optical-pumping are limited because of higher requirements to shorter ultraviolet (UV) light source, and its device is difficult to integrate and use for mass business promotion [19–21].

Therefore, we utilized electron beam (EB) pumping to solve the abovementioned problems [22–24] in 2019. This complex pumping method not only utilizes the easy lasing benefits of optical-pumping but also avoids the power gain-bandwidth product constraint of the PN junction. Therefore, herein, we proposed a corona modulation

Received May 18, 2020; accepted July 2, 2020

E-mails: muyining1985@163.com, myn@cust.edu.cn

device structure based on PQD EB pumping and lasing mechanism and analyzed its detailed designing method.

2 PQD EB pumping lasing experiment and mechanism

Although short lifetime is a typical drawback to be solved for PQDs, an increasing number of scientists have widely utilized ligands modification or elemental doping to improve PQD lifetime. In particular, *Small* reported a new synthesis method for manufacturing stable $CsPbBr_3$ PQDs [25]. Based on that research process, we used the $CsPbBr_3$ solution in our experiment as a classical and typical PQDs material. The fabrication process of PQD films is as follows. As shown in Fig. 1, we synthesized $CsPbBr_3$ quantum dots (QDs) in an oil phase protected by an inert gas with cesium oleate and lead bromide as precursors via thermal injection and rapid ion exchange. Following centrifugation and purification through a high-speed centrifuge, we prepared the $CsPbBr_3$ QD solution of all inorganic metals with hexane as the solvent and a concentration of 10 mg/mL emitting green fluorescence. We ultrasonically cleaned the conductive glass (indium tin oxide (ITO)) substrate with acetone, absolute ethanol, and deionized water for 15 min, dried it using a nitrogen gun, and placed it in a drying oven at 80°C for 30 min. We uniformly stirred the prepared QD solution using a magnetic stirrer to obtain a yellow transparent $CsPbBr_3$ QD spin-coating solution. Then, using the glue machine to manufacture the QD films. We dropped the QD spin-coating solution obtained through a one-step spin-coating method on a conductive glass substrate using a special syringe, for which a homogenizing speed of 900 r/min was maintained for 5–10 s before dripping, and a homogenizing speed of 3500 r/min was maintained after dripping for 10–20 s. Finally, the spin-coating yielded a uniformly translucent $CsPbBr_3$ QD film (QDF). We determined the quantity of syringe droplets using a microelectronic analytical balance with a reading accuracy of 0.01 mg. The experiment revealed that under certain conditions, the higher the spin-coating speed, the longer the gelling time, and the thinner the QDF.

Figure 2 shows the lasing experiment and testing method of the $CsPbBr_3$ QD EB pumping. When the

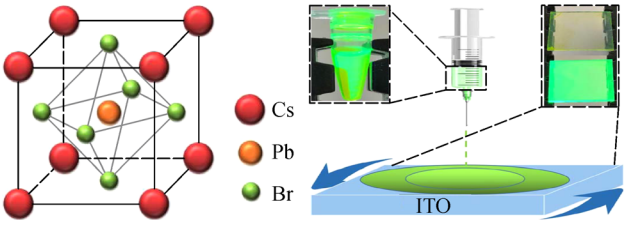

Fig. 1 Crystal structure and thin film preparation process of $CsPbBr_3$

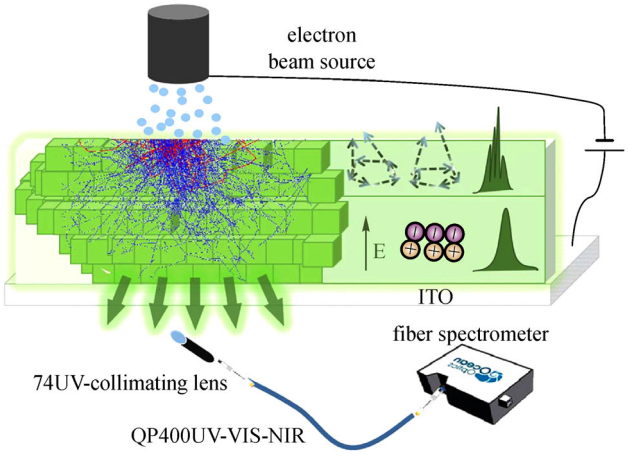

Fig. 2 Lasing experiment of perovskite quantum dot (PQD) electron beam (EB) pumping

pumping voltage between $CsPbBr_3$ QDFs and the EB source reach is strong enough, an increasing number of low-energy particles can absorb sufficient energy from the EB and jump to high energy levels. If the number of stimulated radiation particles considerably outnumbers that of stimulated absorption, the state of the particles is inverted between different energy levels, resulting in massive photon emission. Thus, the process of photon emission is very similar to that of optical pumping of light. Instead of optical pumping, in a vacuum environment, electrons acquire substantial kinetic energy (KE), and the scattering tracks of electrons inside the three-dimensional $CsPbBr_3$ QDFs becomes extremely random because of the EB pumping with extremely strong KE, as shown in Fig. 3. Continual multiple scattering considerably increases the possibility of photons forming feedback loops in space, thereby locally generating resonance to induce random lasing.

To verify the above mechanism, first, we excited the $CsPbBr_3$ QDF using continuous UV light at 365 nm; Fig. 4 shows the spectra obtained at different excitation power densities, which reveal that the emission peak is located at 520 nm, and full width at half maximum (FWHM) is at 20 nm. Second, we designed an original EB pumping device, as shown in Fig. 5. In this photoelectric device, initial photoelectrons from the Au photocathode are triggered using a UV signal. We amplified the photoelectrons to the EB with high energy using a microchannel plate (MCP) to pump $CsPbBr_3$ QDFs under an extra electric field (EF). According to the spectrograph test results shown in Fig. 6, with increasing external voltage between MCP and $CsPbBr_3$ QDFs, the area near the center of the gain curve is preferentially amplified, indicating that the portion of the line width is significantly narrowed, and lasing occurs. When the external voltage exceeds a certain threshold (3 kV), a spike appears in the emission spectrum. When we further increased the external voltage to 5 kV, a narrower

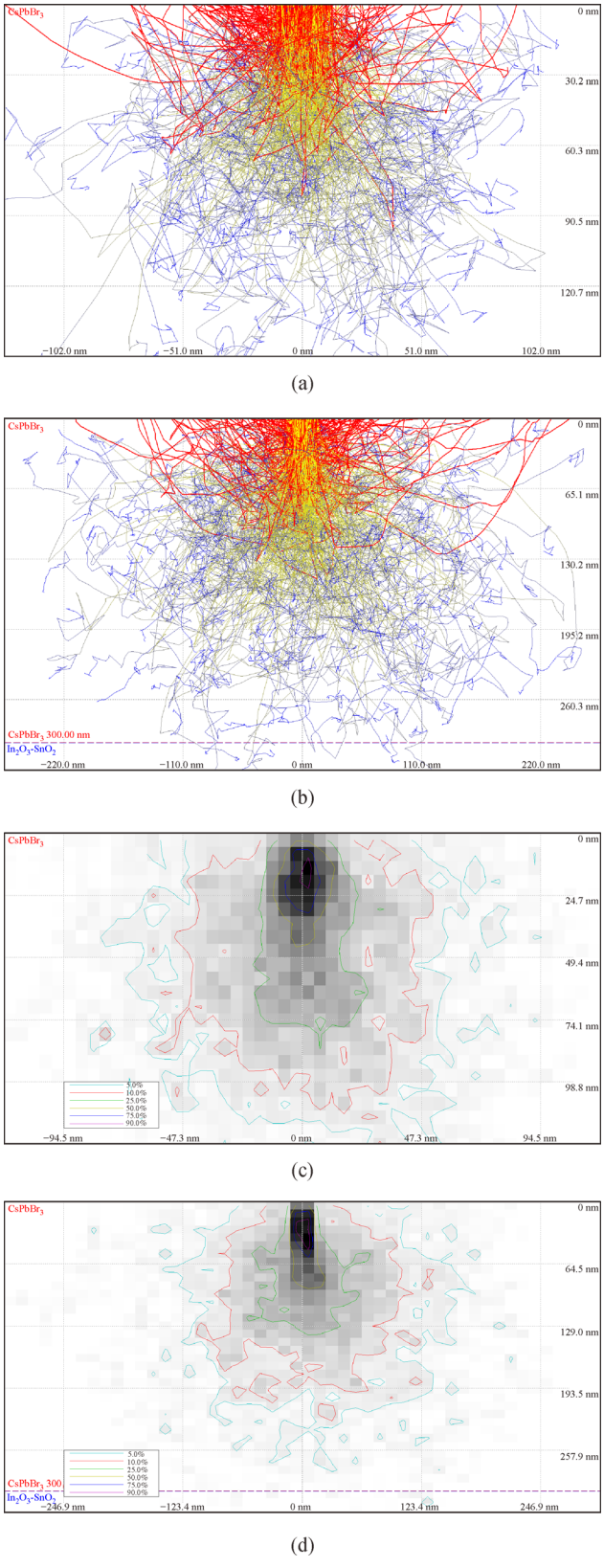

Fig. 3 Scattering effect of EB in a 300 nm thickness PQD film. (a) 3 kV energy EB. (b) 5 kV energy EB. (c) 3 kV energy EB distribution within the PQD film. (d) 5 kV energy EB distribution within the PQD film

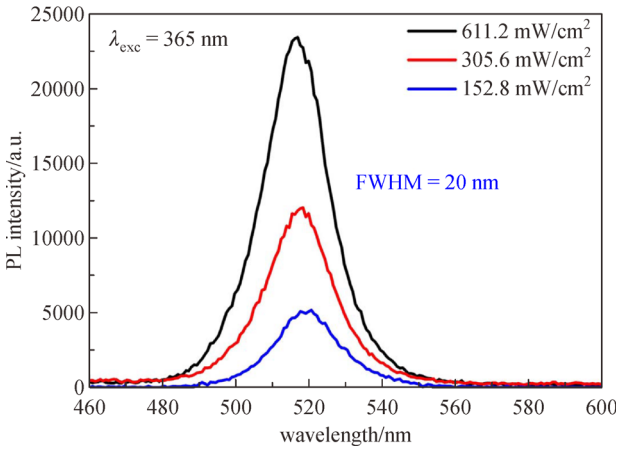

Fig. 4 Photoluminescence (PL) spectra of $CsPbBr_3$ quantum dot thin films

peak appeared, as shown in Fig. 6. At this time, the FWHM of the lasing remained 1 nm or less, which is 1/20 of the half-width of the photoluminescence of the QDF shown in Fig. 4. Figure 7 shows that the number of resonance peaks of the lasing increases with the EB pumping power, and the resonance mode pitch is not uniform, which is characteristic of a typical random laser (RL) mode. Moreover, RL does not need to add a resonant cavity, confirming the feasibility of EB pumped $CsPbBr_3$ QD gain dielectric film random lasing.

Additionally, according to Fig. 7, we note that the RL and feedback model directly depend on the relationships between the thickness of PQD films and external voltage. Because we only tested the transmission spectrum of the random lasing at PQDs' bottom, the thickness of the PQD films significantly affects the test results of the RL and feedback model. Based on Figs. 3 and 7, when PQD films are very thick or around 1000-nm-thick, the majority of the coherent feedback appears at the top of PQD films, and with the deepening of EB bombarding depth, the rate of coherent feedback rapidly decreases. However, incoherent feedback appears at the bottom of PQD films. In Figs. 3(c) and 3(d), the KE of EB distribution located at the top of the PQD films is far stronger than that at the bottom, generating majority feedback loop distribution at the top of the PQD films. Therefore, we believe the RL and feedback model should be complex. Theoretically, the coherent and incoherent feedback should exist simultaneously. Moreover, both model feedbacks are distributed in the entire PQD film. For example, when the PQD films is around 300-nm-thick and the external voltage is around 5 kV, the coherent RL (CRL) whose linewidth is smaller than 1 nm is exactly tested from the bottom of the PQD films, as shown in Fig. 6. However, once the thickness of PQD films increases, the threshold value of lasing is immediately postponed, as shown in Fig. 7, and testing the

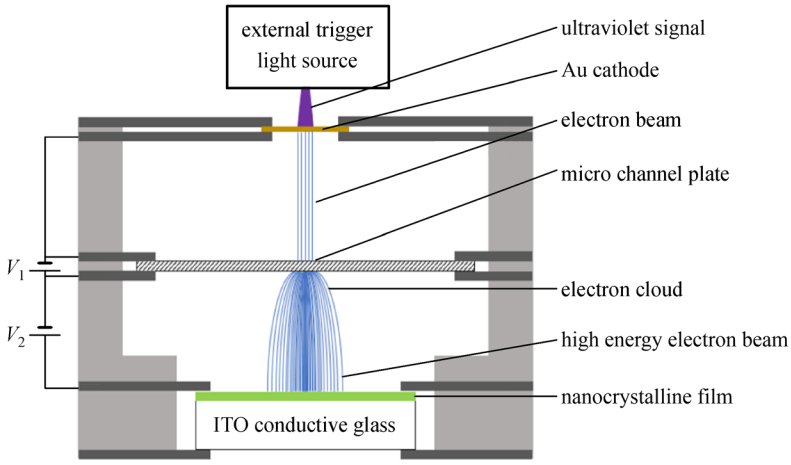

Fig. 5 Original EB pumping device

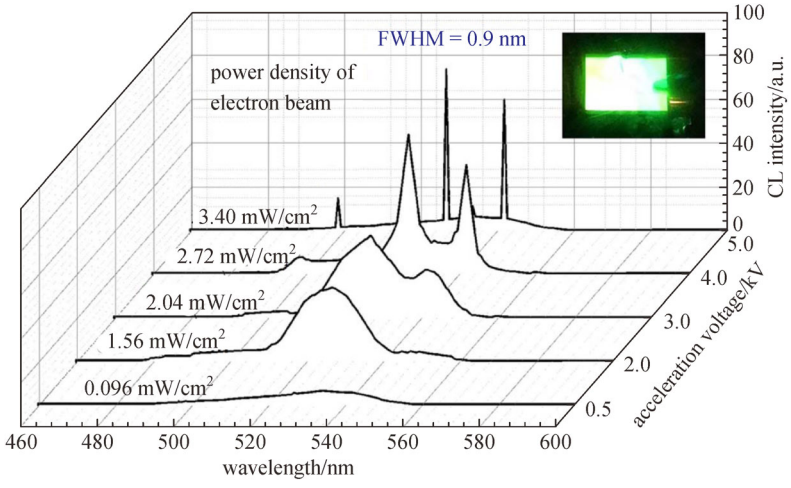

Fig. 6 Lasing effect of PQDs EB pumping. CL, cathodoluminescence

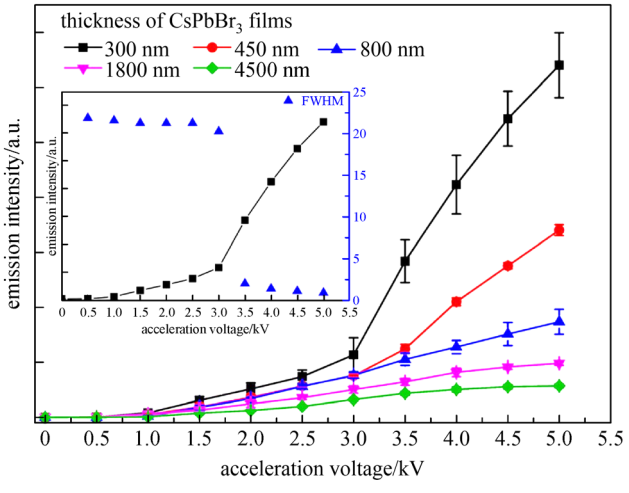

Fig. 7 Relationships between the thickness of PQD films and the external voltage

CRL from the bottom of the PQD films under the same external voltage is very difficult. Finally, with the incidence depth of the EB increasingin the $CsPbBr_3$ QDFs, the KE of the EB and probability of shaped feedback loops rapidly decline, considerably increasing the probability of yielding RL at the top of $CsPbBr_3$ QDFs than at the bottom. Furthermore, even though there is uncertainty of EB pumping power and invalidation of PQDs can more or less affect the testing error of lasing spectrographs, the error range and luminescent tendency of the 300- and 800-nm-thick films, shown in Fig. 7, reappear in the new lasing model under certain conditions. Particularly pumping currents is around several nanoamps, EB pumping only slightly affects the reproducible characteristics of the lasing model in the vacuum.

Theoretically, optically pumped lasing relies on the excitation beam to realize particle beam inversion to produce excitation light, and the excitation light is randomly scattered inside the QD. When the scattering is

strong enough, continuous multiple scattering enables the retur of the photons to the original scattering point or the formation of a feedback loop (ring cavity), which shapes the local resonance of light and produces an RL. Given that, the EB of $CsPbBr_3$ QDs is very similar to optical pumping. The available KE of an EB in a vacuum environment is much higher than that in a solid, rendering the scattering trajectory of high-energy electrons in the three-dimensional fluorescence layer more random. Therefore, the process of an EB transmitting a QD thin film depending on its KE has a very strong random scattering characteristic, which largely replaces the scattering centers in the gain medium and enhances multiple light scattering. Thus, the probability of forming a ring cavity inside the gain medium is further increased through continuous multiple strong scattering, which makes it easier to happen RLs.

Obviously, the massive random lasing emits from the incident plane that receives the EB. The RL principle limits and restrains the design of the LED and modulation system. For example, how to avoid the electric pumping source or the electric–optical modulation system to hinder the strongest random lasing direction, and how to enhance EB modulation's extinction ratio, power utilization, and some device characteristics Moreover, extreme concentration of the EB's focal point reduces the lifetime of the PQDs films. Thus, optimizing the design of the device structure for a specific lasing principle is crucial.

3 Optimum design and discussion

3.1 Integrated designing

As shown in Fig. 8, the corona-shaped device structure mainly includes four components — a focusing chamber, a cathode electron-emitting system, an EF relay modulated gate, and a PQD anode — integrated into a vacuum device. Therein, the external voltage between the modulated gate and the PQD anode is U_{bd}, the modulated voltage between the cathode electron-emitting system and the modulated gate is U_{bc}, and the cathode field strength is E_b, which contains the E_{bc} generated by the modulated gate and E_{bd} generated by the PQD anode. The main body of the device is the focusing chamber, which we divided into three parts, as shown in Fig. 9.

Theoretically, we can approximate the process of the EB's modulation and transfer in the device structure as an electric–optical projection, which means that the electron image of the cathode electron-emitting system is projected to the surface of the PQD anode. If the EB could be swerved using electric–optical projection, the strongest

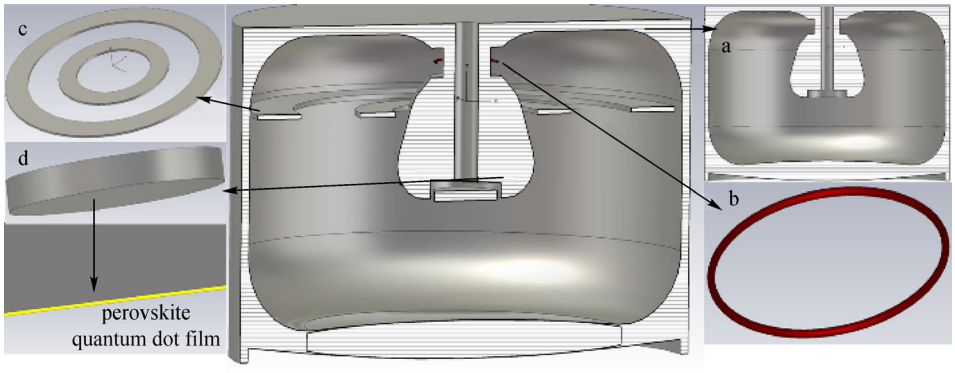

Fig. 8 Corona-shaped EB device structure

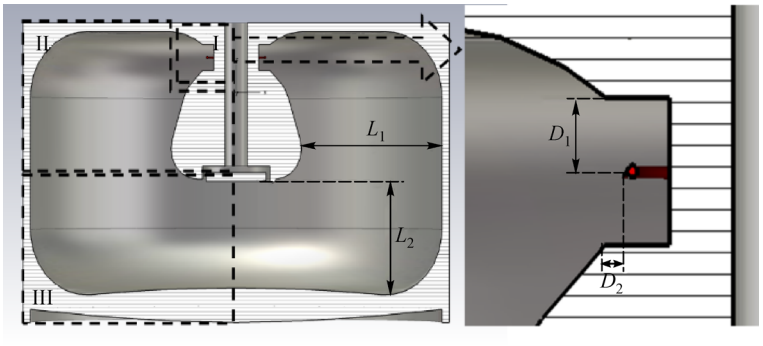

Fig. 9 Ring-shaped focusing chamber structure. L_1 is the diameter of the focusing chamber; L_2 is the length of the focusing chamber in region III; D_1 and D_2 determine the position of the electron source

direction of PQD lasing would be effectively applied. Therefore, the inherent contradiction between the EB pump direction and random lasing direction can be solved using the projection system. However, as an electric–optical projection system, its detailed design parameters such as the matching degree of each subsystem's numerical aperture and field of view (FOV) will directly affect the final EB utilization rate, modulated EB extinction ratio, and other device characteristics.

3.2 FOV matching

Based on the random lasing principle and the above-mentioned inherent contradiction, the external voltage (U_{bd}) should range from 1500 to 5000 eV. Therefore, under a strong EF, we can determine the aperture and curvature of the electric–optical projection by directly using diameter L_1 of the focusing chamber, as shown in Fig. 10. Figure 10 shows the relationships between L_1 and the curvature radius R_x of the electric–optical projection system. In terms of design, to ensure that the FOV of the electric–optical projection system covers as much cathode electron-emitting angle as possible, a design constraint relationship exists between L_1 and R_x. For example, when the pump voltage is around 5000 V in Fig. 10, a tiny L_1 such as 5 or 15 mm restricts the focusing chamber's pupil, which immediately affects the FOV matching and coupling effect of each subsystem and the EB's collection efficiency. Moreover, an excessive L_1 such as 50 mm or more limits R_x and swerve capability to the EB of the electric–optical lens, which subsequently produces the majority of the EB collection by the focusing chamber's wall. Hence, a reasonable range is available for selecting L_1 to match the FOV of each subsystem. For example, Fig. 11 shows a restricted relationship between EB's utilization and L_1 at one scale. Visibly, the optimal value of selecting L_1 ranges from 30 to 35 mm, and we selected the distinguished parameter to accomplish subsequent design and simulation. Four different FOV matching areas exist in a periodical model in terms of FOV matching — off-matching, undermatching, matching, and overmatching FOV areas, respectively. In practice, only when the cathode electron-emitting source is located at the central FOV of the focusing chamber, the matching degree of FOV and collection efficiency of the PQD anode reach their optimum. However, there being an eccentricity angle to FOV matching can effectively avoid the interference from the cathode electron-emitting to the extinction ratio of modulation. Herein, we set the zero FOV at 70° from the center FOV of the focusing chamber. Figure 12 shows several typical eccentricity angles' EB utilization around the zero FOV; a distinguished location with the strongest local EB's utilization appeared at the zero FOV in Fig. 12.

In addition, the electron source's emission angle, 2β, also directly influences the final EB's power utilization, as shown in Fig. 13. Visibly, the larger emission angle 2β effectively enhances the absolute electron output and collection. The PQD anode only collects the part of EB matched between emission FOV and modulated FOV. As shown in Fig. 9, we can approximate the expression of the electron source divergence half-angle β as D_1/D_2; around 1.6 rad appeared as the optimal matching effect in the local matching region.

3.3 Modulation mechanism

Typically, the carrier lifespan of PQDs is ultrashort; thus, its afterglow delay little affects the device's modulated characteristics [26]. The modulated voltage U_{bc} effectively and rapidly changes the distribution of EF measured as several thousand volts (U_{bd}) around the cathode electron-emitting system. Therefore, the modulated gate's designing parameters play a critical role in device designing. Namely, the designing details of the modulated gate directly impact the distribution of EB pumping EF, as shown in Fig. 14, where the L_1 = 35 mm, α is located at the central FOV, and 2β reaches 1.6 rad. The function of the EF relay modulated gate installed in the focusing chamber is to relay or isolate EB pumping EF by changing the modulated voltage (U_{bc}). Theoretically, the modulated gate can be equivalent to add an electron–optical stop controlled by the U_{bc} to affect the matching effect among subsystems. By comparing the EF distribution between Figs. 14(b) and 14(c), the aperture of the entire projection system can be

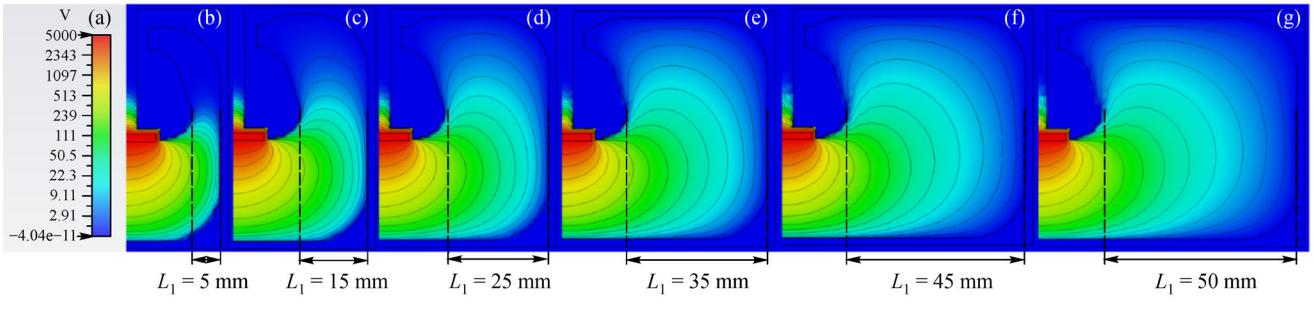

Fig. 10 Field distribution of focusing chamber. (a) Voltage scale. (b) L_1 = 5 mm. (c) L_1 = 15 mm. (d) L_1 = 25 mm. (e) L_1 = 35 mm. (f) L_1 = 45 mm. (g) L_1 = 50 mm

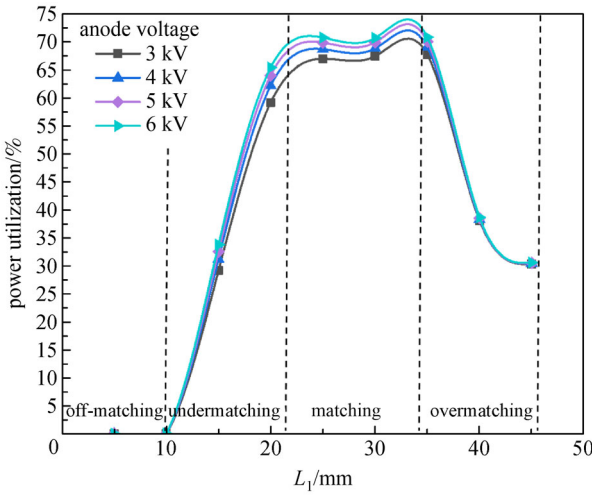

Fig. 11 Field of view (FOV) matching process

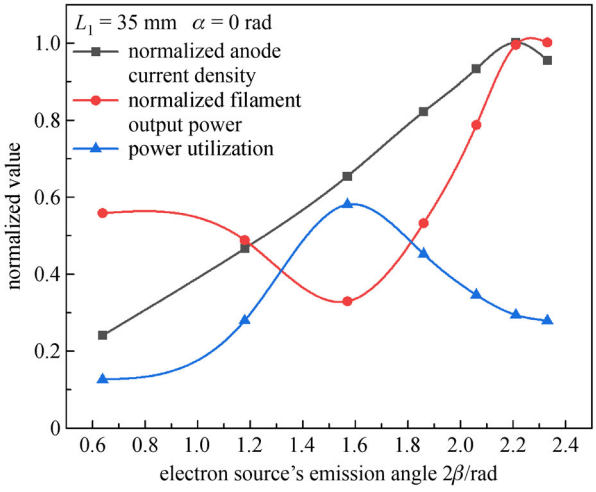

Fig. 13 Electron source's emission angle 2β on FOV matching

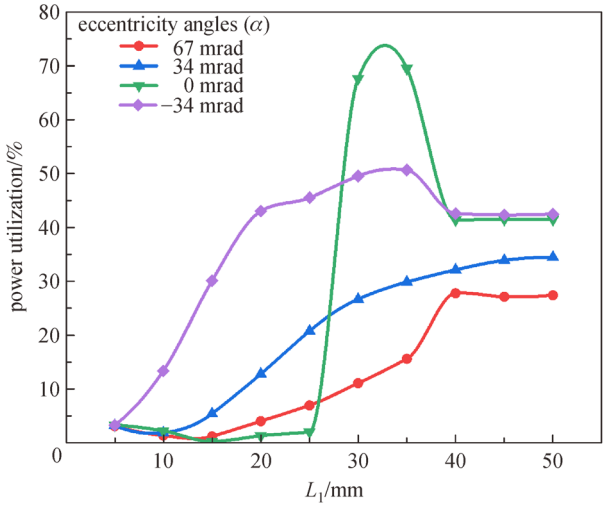

Fig. 12 EB's utilization around the zero FOV

effectively altered by changing the U_{bc}. For example, in Fig. 14(b), when entering into the isolation model, the aperture of the projection system can be markedly cut down, which is equivalent to L_1 decreasing along the x-axis in Fig. 11. Therefore, the essence of this modulation process is to change the efficiency of the PQD anode to collect EB by changing the degree of numerical aperture matching between the modulated gate and the cathode electron-emitting system. Further, to achieve transient modulation and to resist the several thousand volts simultaneously pumping voltage, the modulated voltage U_{bc} should be less than 10 V; the modulated gate's concrete design parameters such as the structure and space of the gate in the projection system are also crucial.

Figure 15 shows some details of the EF relay modulated gate. The modulated gate's vertical distance X and eccentric distance Y will directly determine the object–image relationships and object distance of the projection system; thus, affecting the final numerical aperture matching and eccentricity angle α. Because of the existence of an eccentricity angle in this electric–optical projection, the modulated gate's vertical distance X satisfies the eccentric constraint condition. That is, the influence of the modulated voltage U_{bc} on the electron source can be amplified by a shorter X. However, the electron image of the cathode electron-emitting system and numerical aperture matching will also be affected by a shorter X, and once we add the modulated gate to the entire electronic optical system, the gate will become the aperture

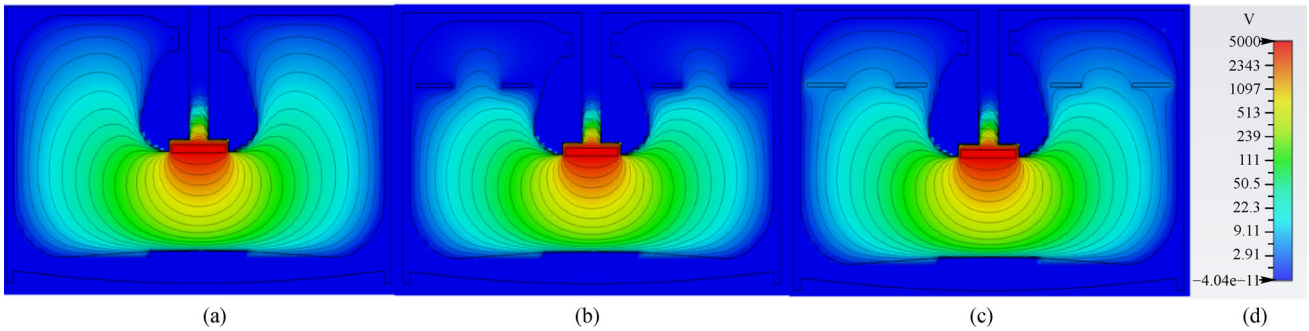

Fig. 14 Working mechanism of modulated gate. (a) Initial model. (b) Isolation model. (c) Relay model. (d) Field scale

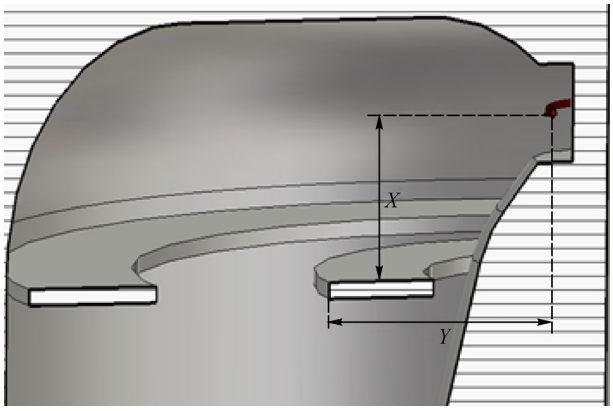

Fig. 15 Concrete details of modulated gate

stop of the projection system, rather than the diameter L_1 of the focusing chamber. Additionally, as the diameter (R) of the aperture stops, the difference between the inner and outer diameters of the modulated gate will influence the number of electrons entering into the projection system. Figure 16 shows the relationships between the modulated EB's utilization ratio and R under different object–image structure. The trend in Fig. 16 is very similar to the process of the FOV matching showing in Fig. 11. Similarly, the eccentric distance Y mainly affects the eccentricity between the modulated gate and the electric–optical projection. Hence, there is an optimal matching location when the center of the modulated gate is located around the center of the focusing chamber. In terms of modulation, excessive X can not only reduce the influence of the modulated voltage U_{bc} on the cathode electron-emitting system but also can weaken the barrier of the modulated gate to pumping EF, which immediately causes modulation extinction ratio's decline under same modulated voltage. Figure 17 shows the effect of the gate's space location and structure on the device modulation characteristics. If the modulation components selected optimal design parameters, for example, the vertical distance is around 11 mm, R is around 19 mm, and the eccentric distance Y is around

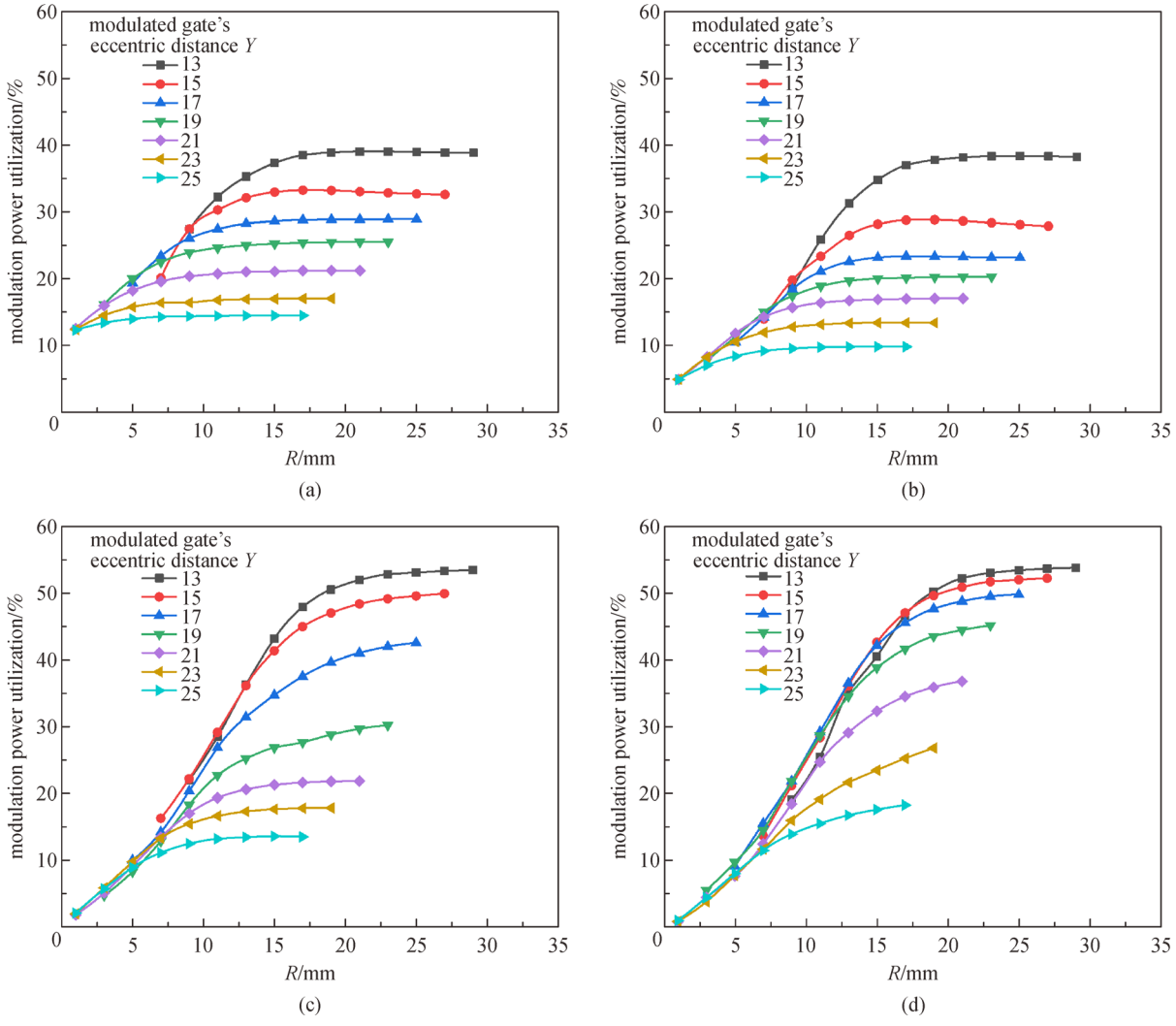

Fig. 16 Influence modulated gate's parameters on EB utilization. (a) X = 6 mm. (b) X = 8 mm. (c) X = 11 mm. (d) X = 13 mm

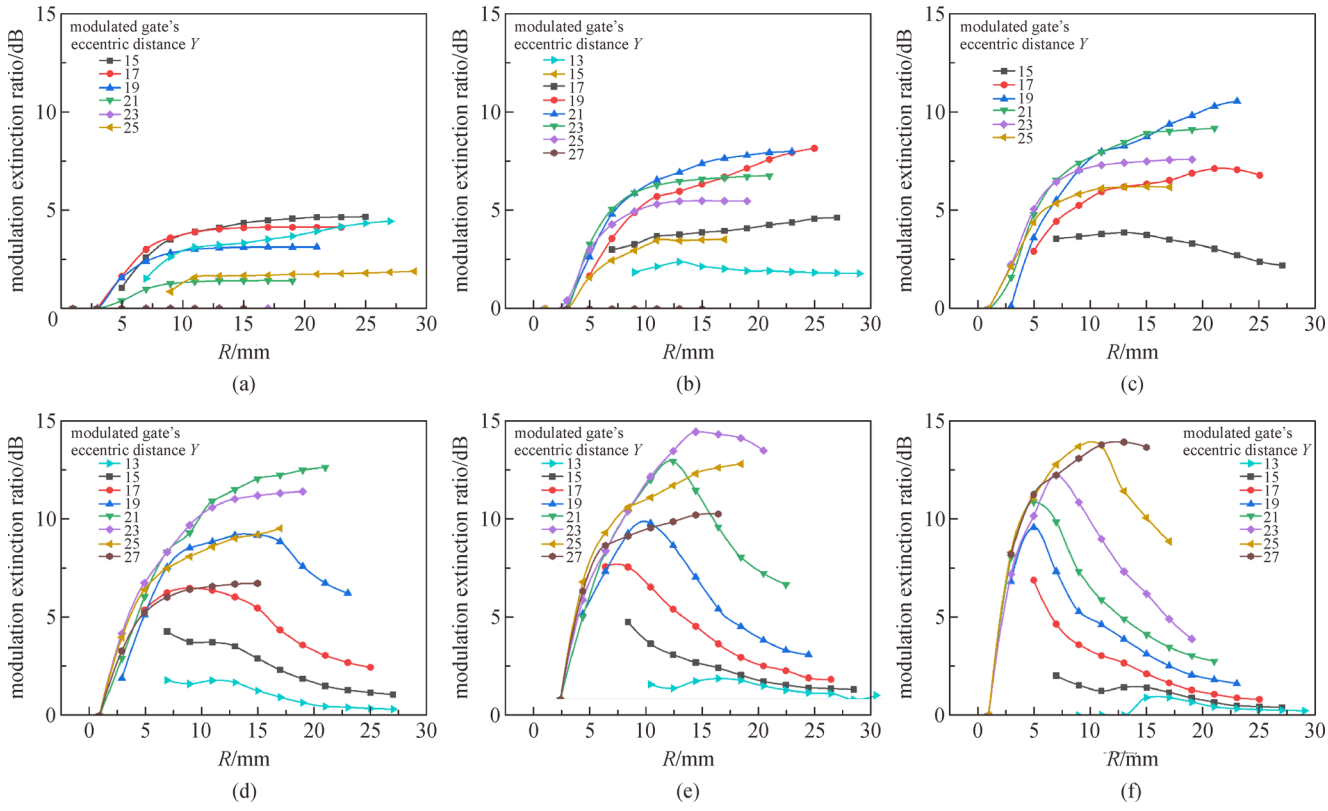

Fig. 17 Influence modulated gate's parameters on EB utilization. (a) $X = 8$ mm. (b) $X = 9$ mm. (c) $X = 10$ mm. (d) $X = 11$ mm. (e) $X = 12$ mm. (f) $X = 13$ mm

20 mm, its extinction ratio can reach an optimum of more than 12 dB. Finally, Fig. 18 shows the EB's utilization of different modulated voltages U_{bc} under the above device optimal parameters. Obviously, based on the modulation structure's optimization design, we need only 3 V to effectively affect the distribution of the EB pumping EF, which considerably enhances the modulator's instantaneous pumping capability in very high-frequency levels.

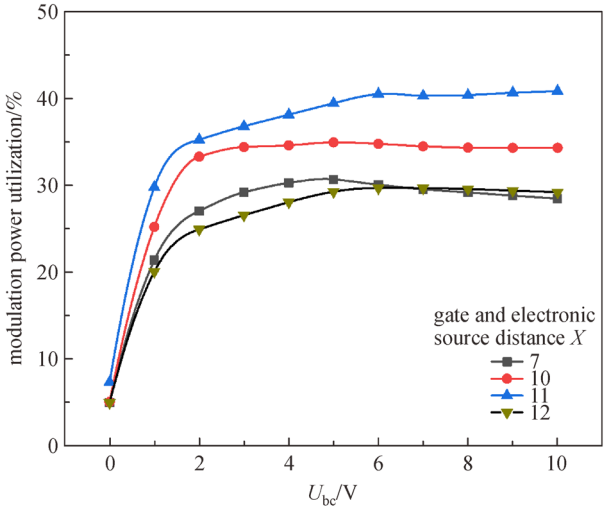

Fig. 18 Relationship between U_{bc} and modulation ability

Finally, to balance the power and modulation characteristics of the EB pumping, Fig. 19 shows static operating points of the corona-shaped EB device structure. We can see that the extinction ratio and power utilization of the modulation component can meet 12 dB and 45% simultaneously at the start, as shown in Fig. 19, using the above optimum design. Moreover, the length of L_2 in region III can also determine the object–image relationships such as principal distance and electronic optics magnification. Figures 20 and 21 show EB's focusing process and final focusing morphology under different lengths of L_2. Excessive EB density will immediately lead to local heat, which greatly reduces the lifetime of the PQDs film. Hence, the final electron spot's energy should be covered on the surface of the PQDs film by accurately controlling L_2 around 28 mm. The final EB focus effect and morphology can be used to evaluate device lifetime of the device optimum design.

4 Conclusions

Summarily, we have the following two conclusions. First, we briefly described PQD lasing under the EB pumping lasing principle. Compared with the optical pump mode,

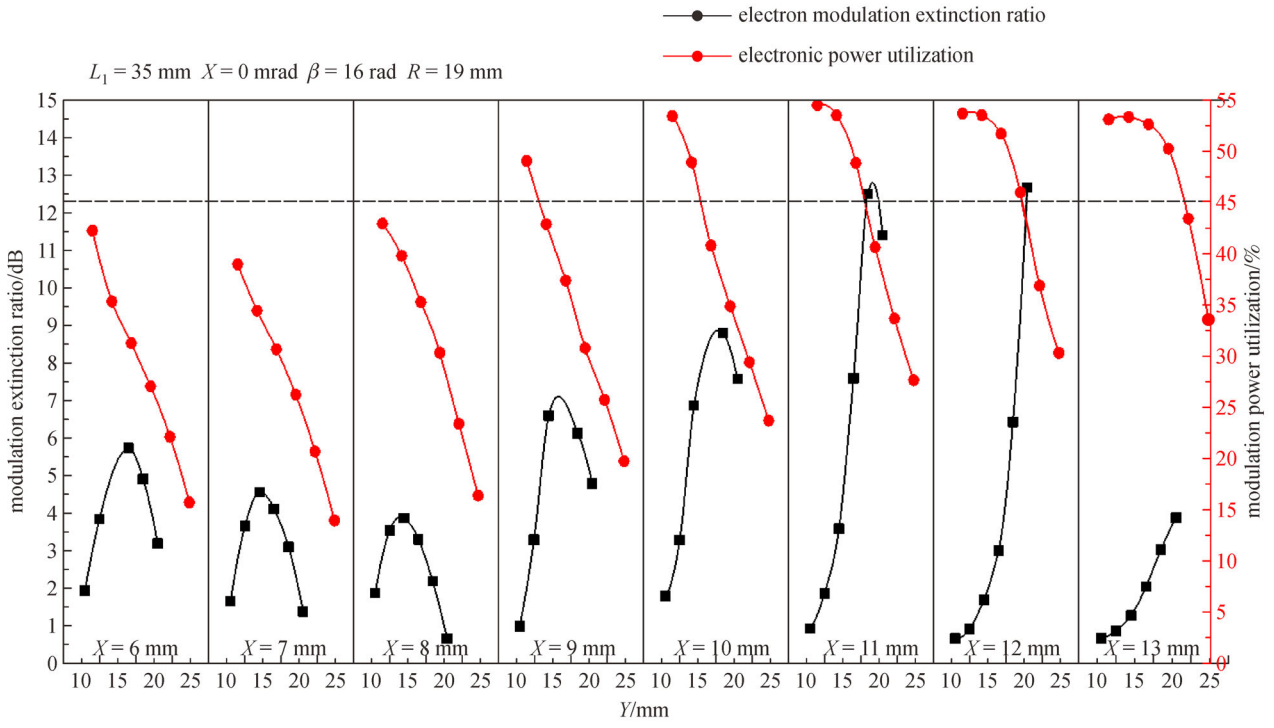

Fig. 19 Static operation points for modulation

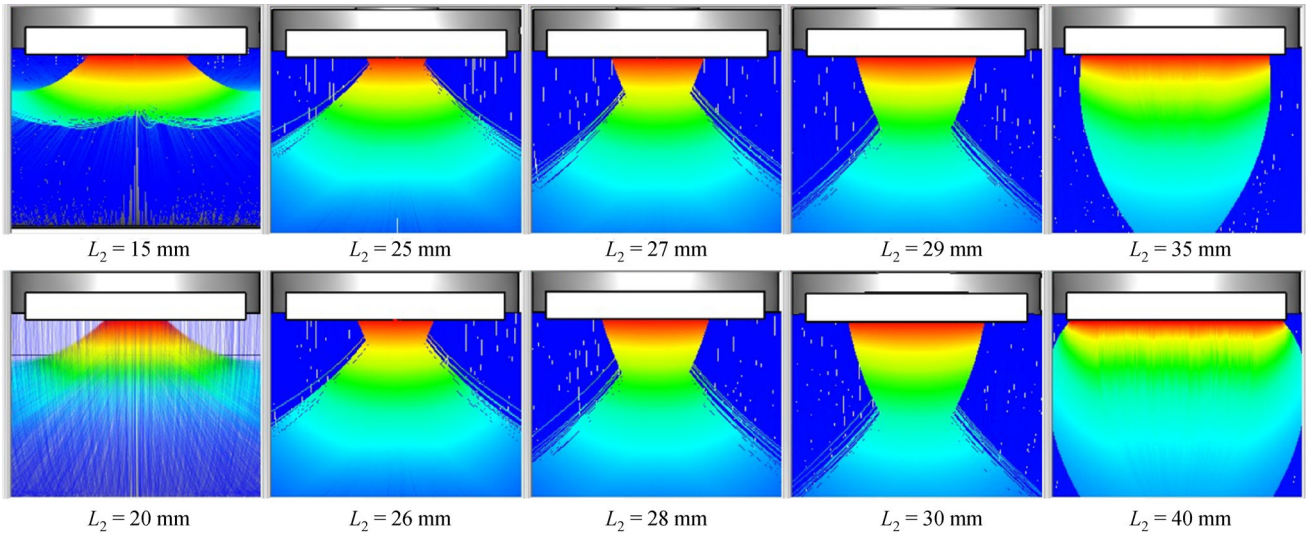

Fig. 20 EB focusing process

the EB pumping mode has distinguished pumping efficiency because the electrons can generate much more KE in the vacuum than the photons, which is easier to realize modulation. Moreover, compared with the LED model, EB's power and KE are mainly from the external EFs; hence, less pumping currents will effectively avoid unnecessary heating of the device, which immediately improves PQD films' lifetime. Further, vacuum environments can effectively isolate oxygen and vapor and slow cluster effect of PQD films and its composition's changing, so that stability of the PQD films can be significantly improved. The pump model for PQD lasing will have very large scientific potential and engineering prospects. Second, based on the random lasing principle of PQD EB pumping, an optimal designing problem between pumping and lasing direction should be solved; therefore, we proposed a corona modulation device model. By simulating and analyzing the FOV matching, modulated

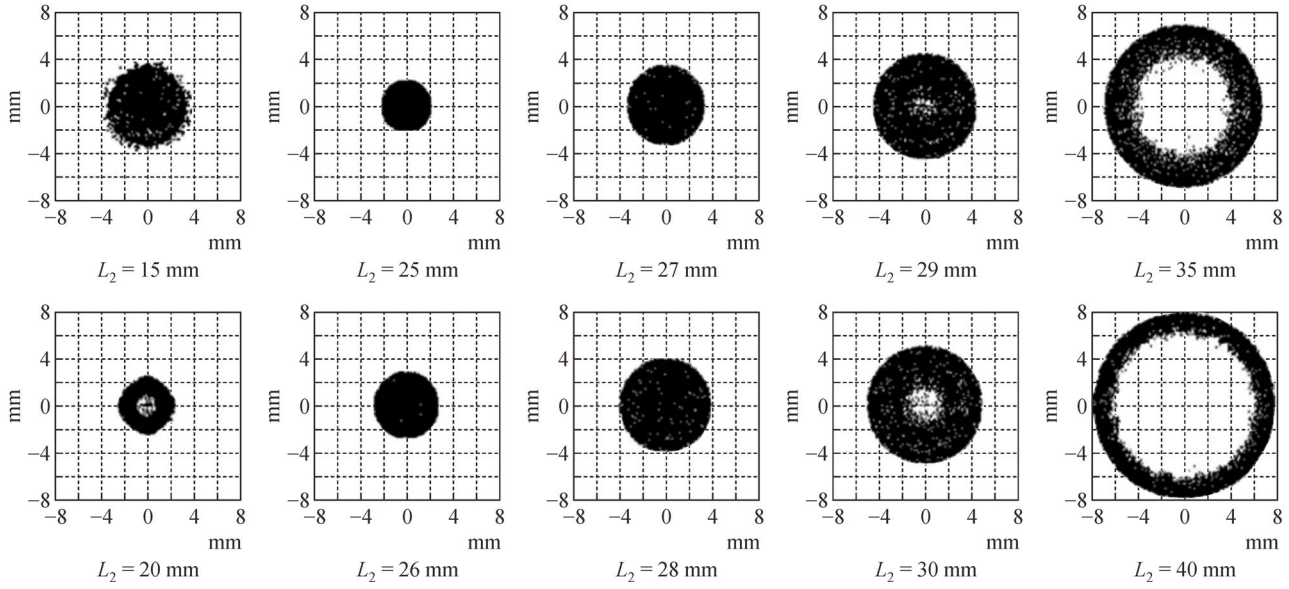

Fig. 21 EB focusing morphology

constraints, electric–optical imaging transfer, and so on of the new device designing method, we revealed its optimal designing method and characteristics. The new EB pumping device model can not only give full play to the advantages of PQD random lasing in the scientific field, but also can directly provide device support for the development of a visible light communication system.

Acknowledgements This work was supported by the National Natural Science Foundation of China (NSFC) (Grant Nos. 51602028, 61905026, and 11874091), Jilin Province Science and Technology Development Project (Nos. 20200301065RQ and 20190701024GH), Chinese Academy of Sciences (No. CAS-KLAOT-KF201803), and Changchun University of Science and Technology (No. XJJLG-2017-01).

References

1. Li C, Zang Z, Han C, Hu Z, Tang X, Du J, Leng Y, Sun K. Highly compact $CsPbBr_3$ perovskite thin films decorated by ZnO nano particles for enhanced random lasing. Nano Energy, 2017, 40(8): 195–202
2. Dong R, Fang Y, Chae J, Dai J, Xiao Z, Dong Q, Yuan Y, Centrone A, Zeng X C, Huang J. High-gain and low-driving-voltage photodetectors based on organolead triiodide perovskites. Advanced Materials, 2015, 27(11): 1912–1918
3. Veldhuis S A, Boix P P, Yantara N, Li M, Sum T C, Mathews N, Mhaisalkar S G. Perovskite materials for light-emitting diodes and lasers. Advanced Materials, 2016, 28(32): 6804–6834
4. Zhang Q, Yin Y. All-inorganic metal halide perovskite nanocrystals: opportunities and challenges. ACS Central Science, 2018, 4(6): 668–679
5. Wei Y, Cheng Z, Lin J. An overview on enhancing the stability of lead halide perovskite quantum dots and their applications in phosphor-converted LEDs. Chemical Society Reviews, 2019, 48(1): 310–350
6. Dong Q, Fang Y, Shao Y, Mulligan P, Qiu J, Cao L, Huang J. Electron-hole diffusion lengths > 175 μm in solution-grown $CH_3NH_3PbI_3$ single crystals. Science, 2015, 347(6225): 967–970
7. Ha S T, Su R, Xing J, Zhang Q, Xiong Q. Metal halide perovskite nanomaterials: synthesis and applications. Chemical Science (Cambridge), 2017, 8(4): 2522–2536
8. Zhang Y, Wu G, Liu F, Ding C, Zou Z, Shen Q. Photoexcited carrier dynamics in colloidal quantum dot solar cells: insights into individual quantum dots, quantum dot solid films and devices. Chemical Society Reviews, 2020, 49(1): 49–84
9. Kodaimati M S, Wang C, Chapman C, Schatz G C, Weiss E A. Distance-dependence of interparticle energy transfer in the near-infrared within electrostatic assemblies of PbS quantum dots. ACS Nano, 2017, 11(5): 5041–5050
10. Bergren M R, Palomaki P K B, Neale N R, Furtak T E, Beard M C. Size-dependent exciton formation dynamics in colloidal silicon quantum dots. ACS Nano, 2016, 10(2): 2316–2323
11. Lee K H, Han C Y, Kang H D, Ko H, Lee C, Lee J, Myoung N, Yim S, Yang H. Highly efficient, color-reproducible full-color electroluminescent devices based on red/green/blue quantum dot-mixed multilayer. ACS Nano, 2015, 9(11): 10941–10949
12. Xiao Z, Bi C, Shao Y, Dong Q, Wang Q, Yuan Y, Wang C, Gao Y, Huang J. Efficient, high yield perovskite photovoltaic devices grown by interdiffusion of solution-processed precursor stacking layers. Energy & Environmental Science, 2014, 7(8): 2619–2623
13. Guan H, Zhao S, Wang H, Yan D, Wang M, Zang Z. Room temperature synthesis of stable single silica-coated $CsPbBr_3$ quantum dots combining tunable red emission of Ag-In-Zn-S for high-CRI white light-emitting diodes. Nano Energy, 2020, 67(1): 104279
14. Sun C, Zhang Y, Ruan C, Yin C, Wang X, Wang Y, Yu W W. Efficient and stable white LEDs with silica-coated inorganic perovskite quantum dots. Advanced Materials, 2016, 28(45):

10088–10094
15. Tang X, Hu Z, Chen W, Xing X, Zang Z, Hu W, Qiu J, Du J, Leng Y, Jiang X, Mai L. Room temperature single-photon emission and lasing for all-inorganic colloidal perovskite quantum dots. Nano Energy, 2016, 28(2): 462–468
16. Wang H C, Lin S Y, Tang A C, Singh B P, Tong H C, Chen C Y, Lee Y C, Tsai T L, Liu R S. Mesoporous silica particles integrated with all-inorganic $CsPbBr_3$ perovskite quantum-dot nanocomposites (MP-PQDs) with high stability and wide color gamut used for backlight display. Angewandte Chemie International Edition, 2016, 55(28): 7924–7929
17. Dursun I, Shen C, Parida M R, Pan J, Sarmah S P, Priante D, Alyami N, Liu J, Saidaminov M I, Alias M S, Abdelhady A L, Ng T K, Mohammed O F, Ooi B S, Bakr O M. Perovskite nanocrystals as a color converter for visible light communication. ACS Photonics, 2016, 3(7): 1150–1156
18. Rainò G, Becker M A, Bodnarchuk M I, Mahrt R F, Kovalenko M V, Stöferle T. Superfluorescence from lead halide perovskite quantum dot superlattices. Nature, 2018, 563(7733): 671–675
19. Kang J, Wang L W. High defect tolerance in lead halide perovskite $CsPbBr_3$. Journal of Physical Chemistry Letters, 2017, 8(2): 489–493
20. Lin K, Xing J, Quan L N, de Arquer F P G, Gong X, Lu J, Xie L, Zhao W, Zhang D, Yan C, Li W, Liu X, Lu Y, Kirman J, Sargent E H, Xiong Q, Wei Z. Perovskite light-emitting diodes with external quantum efficiency exceeding 20 percent. Nature, 2018, 562(7726): 245–248
21. Pan S, Deka S, Amili A E, Gu Q, Fainman Y. Nanolasers: Second-order intensity correlation, direct modulation and electromagnetic isolation in array architectures. Progress in Quantum Electronics, 2018, 59(3): 1–18
22. Fan H, Mu Y, Liu C, Zhu Y, Liu G, Wang S, Li Y, Du P. Random lasing of $CsPbBr_3$ perovskite thin films pumped by modulated electron beam. Chinese Optics Letters, 2020, 18(1): 011403
23. Mu Y, Zhang T, Chen T, Tang F, Yang J, Liu C, Chen Z, Zhao Y, Du P, Fan H, Zhu Y, Liu G, Li P. Manufacturing and characterization on a three-dimensional random resonator of porous silicon/TiO_2 nanowires for continuous light pumping lasing of perovskite quantum dots. Nano, 2020, 15(02): 2050016
24. Du P, Mu Y, Ren H, Fan H, Zhu Y, Li Y, Idelfonso M. Transient luminescence characteristics of random laser emission based on electron beam pumping perovskite nanocrystals. Acta Photonica Sinica, 2020, 49(04): 146–152
25. Yan D, Shi T, Zang Z, Zhou T, Liu Z, Zhang Z, Du J, Leng Y, Tang X. Ultrastable $CsPbBr_3$ perovskite quantum dot and their enhanced amplified spontaneous emission by surface ligand modification. Small, 2019, 23(15): 1901173
26. Wang H, Zhang P, Zang Z. High performance $CsPbBr_3$ quantum dots photodetectors by using zinc oxide nanorods arrays as an electron-transport layer. Applied Physics Letters, 2020, 116(16): 162103

Yan Zhu is currently a doctoral candidate in Department of Electronic Science and Technology, Changchun University of Science and Technology, China. His main research direction is white optical communication system and optoelectronic devices.
E-mail: zhuyan6338@163.com

Yining Mu is currently a full professor and doctoral supervisor at Changchun University of Science and Technology, China. His research interests include space optical-communication and optoelectronic devices.
E-mails: muyining1985@163.com, myn@cust.edu.cn

Fanqi Tang is currently a M.S. candidate in Department of Electronic Science and Technology, Changchun University of Science and Technology, China. His research direction is electronic science and technology.
E-mail: 32506933@qq.com

Peng Du is currently a M.S. candidate in Department of Electronic Science and Technology, Changchun University of Science and Technology, China. His research direction is optical communication and optoelectronic devices.
E-mail: 68254899@qq.com

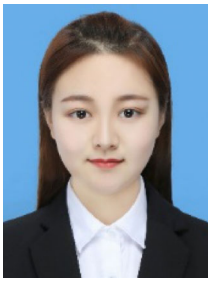

Hang Ren is currently a M.S. candidate in Department of Electronic Science and Technology, Changchun University of Science and Technology, China. Her research direction is optical communication and optoelectronic devices.
E-mail: 1579945753@qq.com